MATERIALS SCIENCE

Direct writing of customized structural-color graphics with colloidal photonic inks

Jong Bin Kim[1], Changju Chae[2], Sang Hoon Han[1], Su Yeon Lee[2], Shin-Hyun Kim[1]*

Colloidal crystals and glasses have been designed to develop structural colors that are tunable, iridescent, nonfading, and nontoxic. However, the low printability and poor printing quality have restricted their uses. Here, we report the direct writing of structural-color graphics with high brightness and saturation using colloidal inks. The inks are prepared by dispersing silica particles in acrylate-based resins, where the volume fraction is optimized to simultaneously provide pronounced coloration and satisfactory printing rheology. With the inks, any macroscopic design of lines and faces can be directly written on various substrates, where the microscopic colloidal arrangement is set to be either crystalline or amorphous depending on the resin viscosity to control the iridescence of the colors. In addition, the high mechanical stability and controlled modulus enable the graphics to be surface-transferred, origami-folded, or elastically stretched. This direct-writing approach provides unprecedented levels of controllability and versatility for pragmatic uses of structural colors.

INTRODUCTION

Nature has created periodic nanostructures to develop structural colors, which enhance or reduce the visibility of animals for mating competition or camouflage (*1*, *2*). Some plants living in light-deficient environments use nanostructures to improve their photosynthesis efficiency (*3*, *4*). Inspired by nature, researchers have developed artificial periodic nanostructures that provide tunable, iridescent, nonfading, and nontoxic colors (*5*). The preparation of colloidal assemblies is among the most cost-effective and facile methods to produce photonic nanostructures (*6*). Colloidal crystals with long-range order show brilliant colors with strong iridescence (*7*), whereas colloidal glasses with short-range order show relatively faint colors with low angle dependency (*8*, *9*). Using colloidal arrays for practical coloration necessitates the patterning of colloidal arrays with a controlled arrangement and high mechanical stability in a reliable and reproducible manner. Structural-color printing that can be customized according to the design, color combination, and type of target substrate is particularly attractive.

Although various strategies for structural-color patterning with colloidal assemblies have been suggested, few of them simultaneously satisfy the requirements for commercial applications (*10*, *11*). Evaporation-induced self-assembly has been used for colloidal suspensions locally deposited but suffers from low throughput and poor mechanical stability of the resultant pattern (*12*–*16*). Although various top-down lithographic techniques have been used to prepare micropatterns of bottom-up colloidal assemblies, these techniques typically involve delicate and time-consuming multistep processes when used for multicolor patterning (*17*–*22*). Inkjet printing is one of the most promising methods for customizable patterning; however, a large areal fraction of voids and the spherical geometry of the resultant colloidal assemblies limit the color brightness (*23*–*29*). Therefore, it remains as a longstanding challenge to produce structural-color patterns with a high optical performance and sufficient mechanical stability at high throughput through simple and facile processes.

We here report direct writing with colloidal photonic inks for customizable structural-color printing. To avoid a time-consuming evaporation process, particles are rendered to have repulsive interparticle potential in the absence of volatile components, which causes the spontaneous ordering of particles. The inks are optimally formulated by dispersing silica particles in photocurable resins at volume fractions appropriate for both macroscopic printing and microscopic colloidal structuring. The resins are carefully selected to make a solvation layer on the surface of particles for interparticle repulsion and provide the desired mechanical properties. With the inks, lines are directly written by a dispenser, where the width of the lines can be controlled in situ by adjusting the writing speed. Faces are formed by the fusion of lines, which shows negligible surface undulation. The colloidal arrangement in the lines and faces is set to be either a crystalline array for strongly iridescent coloration or an amorphous array for relatively matte coloration according to the viscosity of the resins, which dictates the time scale for colloidal crystallization. The orientation of colloidal crystals in lines and faces is governed by the shear conditions experienced by the inks during and after the printing. The lines show three different crystal orientations in the cross section due to position-dependent shear conditions during ejection from the nozzle and spreading on a target surface. In particular, the fusion of as-printed adjacent lines causes the colloidal crystals in the faces to align parallel along the surfaces, achieving 80% absolute reflectivity. Multicolor graphics are directly written on various substrates, including glasses, plastics, metals, paper, and some fabrics, which are permanently stabilized by photocuring the resins. Paper with graphics is foldable for origami, and the fabrics with graphics are stretchable depending on the ink selected. Also, the graphics can be released from the substrates to prepare freestanding films or to transfer them onto other surfaces. This previously unexplored direct writing approach of colloidal photonic inks will potentially serve as a pragmatic means to create customized structural-color graphics for various purposes.

RESULTS

Ink formulation

The direct-writing process deposits ink materials onto target surfaces along preprogrammed trajectories to produce customized graphics

[1]Department of Chemical and Biomolecular Engineering (BK21 four), Korea Advanced Institute of Science and Technology (KAIST), Daejeon 34141, Republic of Korea. [2]Division of Advanced Materials, Korea Research Institute of Chemical Technology (KRICT), Daejeon 34114, Republic of Korea.
*Corresponding author. Email: kim.sh@kaist.ac.kr

and patterns without masks while minimizing the use of valuable ink (Fig. 1A) (*30*). The printing speed and pattern resolution are predominantly governed by the rheological properties of the inks. A well-defined colloidal arrangement in the form of either crystals or glasses is a prerequisite for structural coloration. Therefore, the formulation of inks is important for the direct writing of structural-color graphics to achieve high resolution, high color quality, and fast printing.

We formulate the inks by dispersing monodisperse silica particles in acrylate-based photocurable resins in the absence of volatile components; carbon black nanoparticles are additionally dispersed in the acrylate resin to reduce Mie scattering. The resins—ethoxylate acrylate (EA), phenyl ether acrylate (PEA), and urethane acrylate (UA)—are carefully screened and selected to have stable and homogeneous dispersions at volume fractions as high as $\phi \sim 0.5$. EA is rigid, PEA is elastic, and UA is tough after photocuring. The resin molecules bind to the surface of silica particles through hydrogen bonds between the acrylate groups of the resins and the silanol groups of silica, forming a solvation layer (Fig. 1B). Because the solvation layers render the silica particles repulsive, the dispersion is highly stable even at ultrahigh silica particle concentrations. Silica particles in all three resins spontaneously form a crystalline lattice in the entire volume when the dispersions are incubated for a sufficiently long time as long as the ϕ is greater than the threshold of $\phi_{th} \sim 0.15$ (fig. S1). Crystallization in EA and PEA requires few minutes for $\phi \sim \phi_{th}$, whereas that in UA requires a few days because the viscosity of UA is two orders of magnitude greater than those of EA and PEA.

The volume fractions of silica particles are optimized for each resin and particle size to simultaneously achieve good printability and a controlled colloidal arrangement. With increasing volume fraction, the dispersions become increasingly viscous and suddenly change to a brittle solid for all three resins (fig. S2). The volume fraction corresponding to the liquid-to-solid transition (ϕ_{tr}) is ~0.53 for EA,

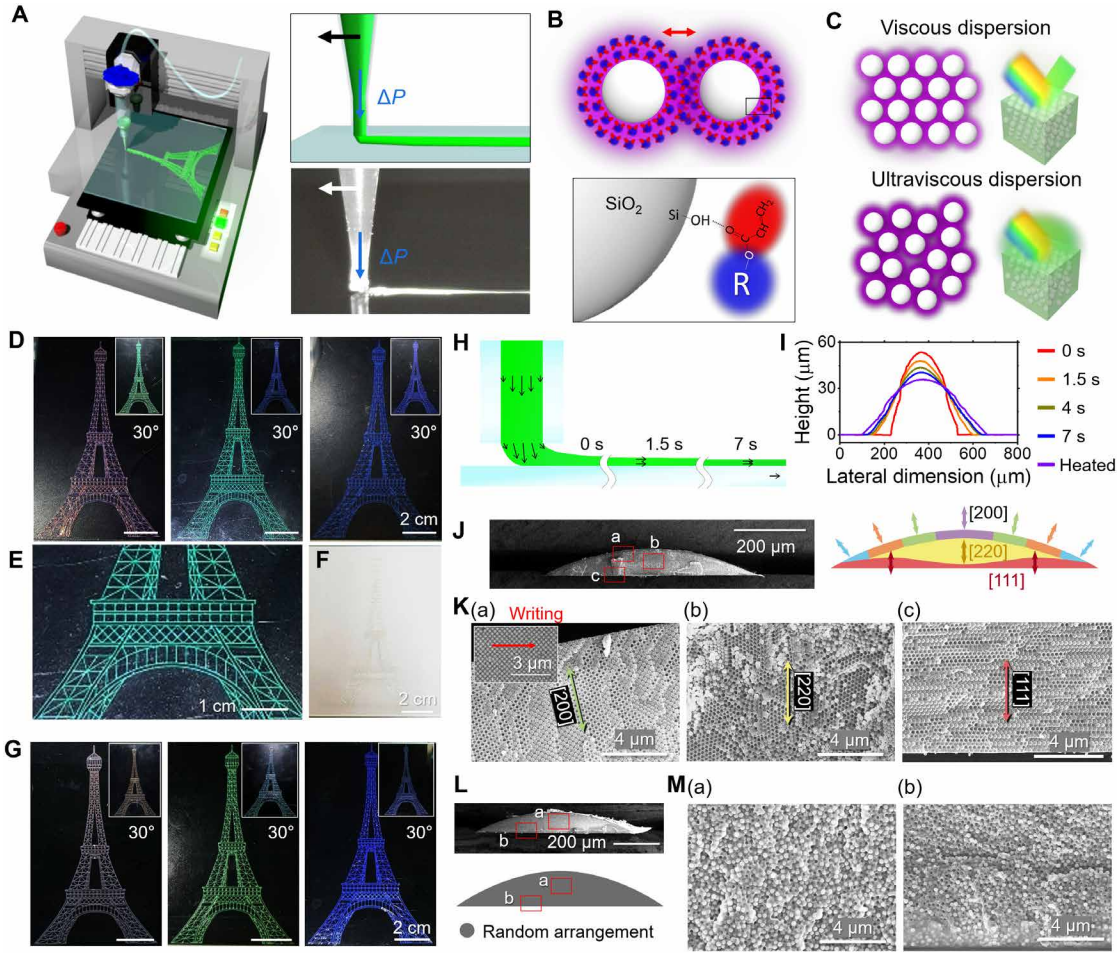

Fig. 1. Direct writing of structurally colored lines. (**A**) Dispenser for line drawing with a moving nozzle. (**B**) Formation of a solvation layer on the silica surface by hydrogen bonds. (**C**) Crystalline and glassy packing in moderately viscous ethoxylate acrylate (EA) and ultraviscous urethane acrylate (UA). (**D** to **F**) Eiffel Tower patterns drawn using EA inks: red, green, and blue colors (D), magnified view (E), and the pattern viewed under off-reflection with a white background (F). The insets are off-normal views for specular reflection. (**G**) Eiffel Tower patterns drawn using UA inks. (**H** and **I**) Velocity profiles of inks (H); temporal evolution of the surface profiles of an EA line (I). (**J** and **K**) Cross-sectional scanning electron microscopy (SEM) images of an EA line and schematic showing position-dependent crystal orientations (J); (200) planes of a face-centered-cubic (fcc) lattice in the top [K(a)], (220) planes in the middle [K(b)], and (111) planes in the bottom [K(c)]. The inset in [K(a)] shows a square array on the top surface. (**L** and **M**) The same set of subfigures as those in (J) and (K) but for a UA line. A consistent amorphous array is formed in the whole volume. Photo credit: Jong Bin Kim, KAIST.

~0.58 for PEA, and ~0.43 for UA when silica particles with a diameter of d = 190 nm are dispersed. The ϕ_{tr} changes to ~0.52 for d = 175 nm and ~0.54 for d = 226 nm in EA and to ~0.40 for d = 145 nm and ~0.45 for d = 226 nm in UA; they are dependent on particle sizes (*31*). The transition occurs when no lubrication layer of free molecules is available among silica particles because most of the resin molecules are strongly bound. Therefore, ϕ_{tr} depends on d, which is approximated as $0.64\left(1+\frac{12.6\,\text{nm}}{d}\right)^{-3}$ for EA, $0.64\left(1+\frac{7.6\,\text{nm}}{d}\right)^{-3}$ for PEA, and $0.64\left(1+\frac{26.6\,\text{nm}}{d}\right)^{-3}$ for UA (fig. S3C). The volume fraction for inks should be set between ϕ_{th} and ϕ_{tr}. However, the dispersions with $\phi \sim \phi_{th}$ are highly fluidic, which causes an overdose even at the minimum controllable pneumatic pressure and resulted in leakage even after the pressure is turned off; both the flow rate and the time scale for stopping Poiseuille flows are inversely proportional to the viscosity. The leakage leads to the formation of dog bone–like drops at the end of lines, degrading the precision of the patterning. In addition, the lines are broadened when they are crossed (fig. S4A). By contrast, the dispersions with $\phi \sim \phi_{tr}$ achieve high precision of patterning but show poor microscopic order of colloidal arrays because of the limited mobility of particles, displaying low color saturation and brightness (fig. S4C). That is, an optimum volume fraction, ϕ_{opt}, exists that enables high printing precision and high color quality; the value of ϕ_{opt} is semi-empirically found to be $\phi_{opt} \sim \phi_{tr} - 0.02$ for all three resins (fig. S5). The inks of EA and PEA resins contain crystalline arrays of silica particles after printing, while that of UA resin has amorphous arrays (Fig. 1C). For EA, PEA, and UA with ϕ_{opt}, the concentration of carbon black in a silica-free resin basis is optimally set to 0.05% (w/w) to enhance the color chroma by suppressing incoherent scattering without compromising the reflectivity (*32*, *33*).

Direct writing of structurally colored lines

We use the optimized EA and UA inks to draw a graphic of the Eiffel Tower (Paris, France) on a glass slide; the inks are loaded into a tapered nozzle with a 200-μm orifice and are pressurized to be ejected, while the nozzle is horizontally moved with a 100-μm gap between the nozzle and slide. The writing speed s is set to be constant at 8 mm s^{-1} with pressures of ΔP = 100 kPa for EA and ΔP = 300 kPa for UA (movie S1). The inks form an arch-shaped cross section: The EA lines show a constant width of 530 μm and a height of 73 μm, and the UA lines exhibit a width of 535 μm and height of 119 μm. The writing of the Eiffel Tower graphic with dimensions of 127 mm by 68 mm requires ~10 min. The printed graphic is thermally incubated at 85°C for 10 min to improve the microscopic order of the silica particles. The Eiffel Tower graphics drawn with EA inks are highly iridescent under specular reflection and highly transparent at the same time under the off-specular condition, whereas those drawn with UA inks show a low angle dependence and a wide viewing angle (Fig. 1, D to F, fig. S6, and movie S2).

The silica particles sequentially experience two different shear conditions. When the inks flow in the nozzle and the gap between the orifice and slide, silica particles rearrange to alleviate the shear stress, causing shear thinning (*34*–*36*); the shear thinning is much stronger for the EA inks than for the UA inks (figs. S7 and S8). The shear-dependent particle arrangement is speculated on the basis of shear-dependent changes of storage and loss moduli and direct observation by capturing colloidal arrangements (figs. S9 and S10) (*37*–*39*). Under the typical printing condition with a shear rate of 10 s^{-1}, silica particles can arrange into strings along the flow direction for the EA inks (*40*, *41*), whereas they form fragmented amorphous arrays for the UA inks. The printing by a moving nozzle can be considered equivalent to printing by a stationary nozzle on a substrate moving in the opposite direction. At the moment of deposition, the velocity profile is approximated by a superposition of the vertical parabolic profile of the Poiseuille flow from the nozzle and the linear horizontal profile of Couette flow at the gap between the nozzle and the moving substrate (Fig. 1H and fig. S11). The dispersion near the top surface of the printed lines exhibits an oblique flow direction, whereas the middle has an almost vertical flow direction. The wall stress from the nozzle is removed discontinuously, which causes a transition to plug flow. Afterward, the dispersion of printed lines spreads along the direction perpendicular to the writing (Fig. 1I). As the viscosity gradually recovers via thixotropic relaxation, spreading is not negligible; the time scale for the thixotropic recovery is ~30 s for the transition from 10 s^{-1} to 10^{-3} s^{-1} for EA and longer than 150 s for UA (figs. S7 and S8). For the EA inks, the shear rate by spreading is approximated as 1.03 s^{-1} for the initial 1.5 s and decreases to 0.52 s^{-1} for the next 2.5 s and 0.39 s^{-1} for the next 3 s; the shear rate is approximated from the temporal change of the cross section of lines (fig. S12). During the spreading, the dispersion in the central area of the line remains shear free, whereas that in the edges experiences shear. The spreading almost stops at 10 s, and no substantial spreading is observed during thermal annealing at 85°C for 10 min. For the UA inks, the shear rate is 0.108 s^{-1} for the initial 3 s, and the spreading proceeds slowly yet steadily for several hours; this behavior differs substantially from that of the EA inks (fig. S13).

The flow condition dictates the orientation of colloidal crystals in the thermally annealed lines for the EA inks. A square array, the (200) plane of a face-centered cubic (fcc) lattice, is observed on the entire top surface of the lines, where its diagonal is parallel to the writing direction [inset of Fig. 1K(a) and fig. S14]. The lattice spans 20% of the entire thickness from the top. This unexpected crystal orientation is caused by the string-like arrangement along the oblique flow field with an angle of approximately 45° in the top region at the moment of deposition. The string-like arrangement evolves to the [220] direction of the fcc lattice along the angle during thermal annealing, resulting in a (200) plane on the top surface. Therefore, the square lattice of the (200) plane is aligned to have a diagonal along the writing direction. Because the dispersion in the middle of the lines experiences a vertical flow field, the [220] direction of the fcc lattice is aligned vertically, taking approximately 70 and 50% of the entire thickness at the center and off-center, respectively [Fig. 1K(b) and fig. S15]. The typical fcc (111) plane is only formed along the bottom surface, which spans 10% of the thickness in the center and increased in thickness (approximately 25 to 30%) with increasing distance from the center [Fig. 1K(c) and fig. S16]. This normal crystal orientation is caused by the shear-induced rearrangement during the spreading, which leads to the formation of a thicker layer near the edge than near the center (fig. S17). The crystalline structures render the graphics printed with EA inks highly transparent. The iridescent structural colors are predominantly developed by the (111) planes on the bottom surface; the (220) planes in the middle have diffraction in UV and (200) planes on the top show relatively weak reflection (fig. S18). By contrast, in the case of the UA inks, the colloids form amorphous arrays with short-range order in the entire volume of the printed lines, including interfaces, even after thermal annealing (Fig. 1, L and M, and fig. S19). The extremely high viscosity prevents the formation of long-range order despite the repulsive

interparticle interaction and shear flow. The short-range order develops faint yet apparent colors, featured by a broad reflectance peak, for wide viewing angles with relatively low angle dependency (fig. S20).

Control over line dimensions in operation window

Straight lines are drawn when the ejection rate of inks from the nozzle is sufficiently high to fill the gap between the nozzle and the target surface while the nozzle is moving. When the ejection rate is too low compared with the writing speed, the inks form a series of dots as they are deposited only when they contact the surface (fig. S21). Dog bone–like drops are formed at the end of lines when the inks leak out even after the pressure is turned off; this effect is exacerbated at higher flow rates because of the stronger shear thinning and is less severe for the UA inks because of weaker shear thinning. Therefore, an optimum window of pneumatic pressure and writing speed exists for a given gap distance (Fig. 2, A and B); the minimum pneumatic pressure for printing using the EA inks is much lower than that for printing using the UA inks because of the stronger shear thinning of the EA inks, although the two inks' viscosities near zero shear are comparable ($\eta \sim 10^6$ mPa·s) (figs. S7 and S8). Within the window, the line width and height are controlled by the pneumatic pressure and the writing speed (Fig. 2, C to F). The cross section of the lines is arch shaped, and the height-to-width ratio of ~0.09 is approximately constant for the EA inks on glass substrates; by contrast, it varies from a typical value of 0.12 according to the gap distance for the UA inks. The gap distance dictates the minimum line width. For the EA inks, the gap determines the volume of ink retained between the

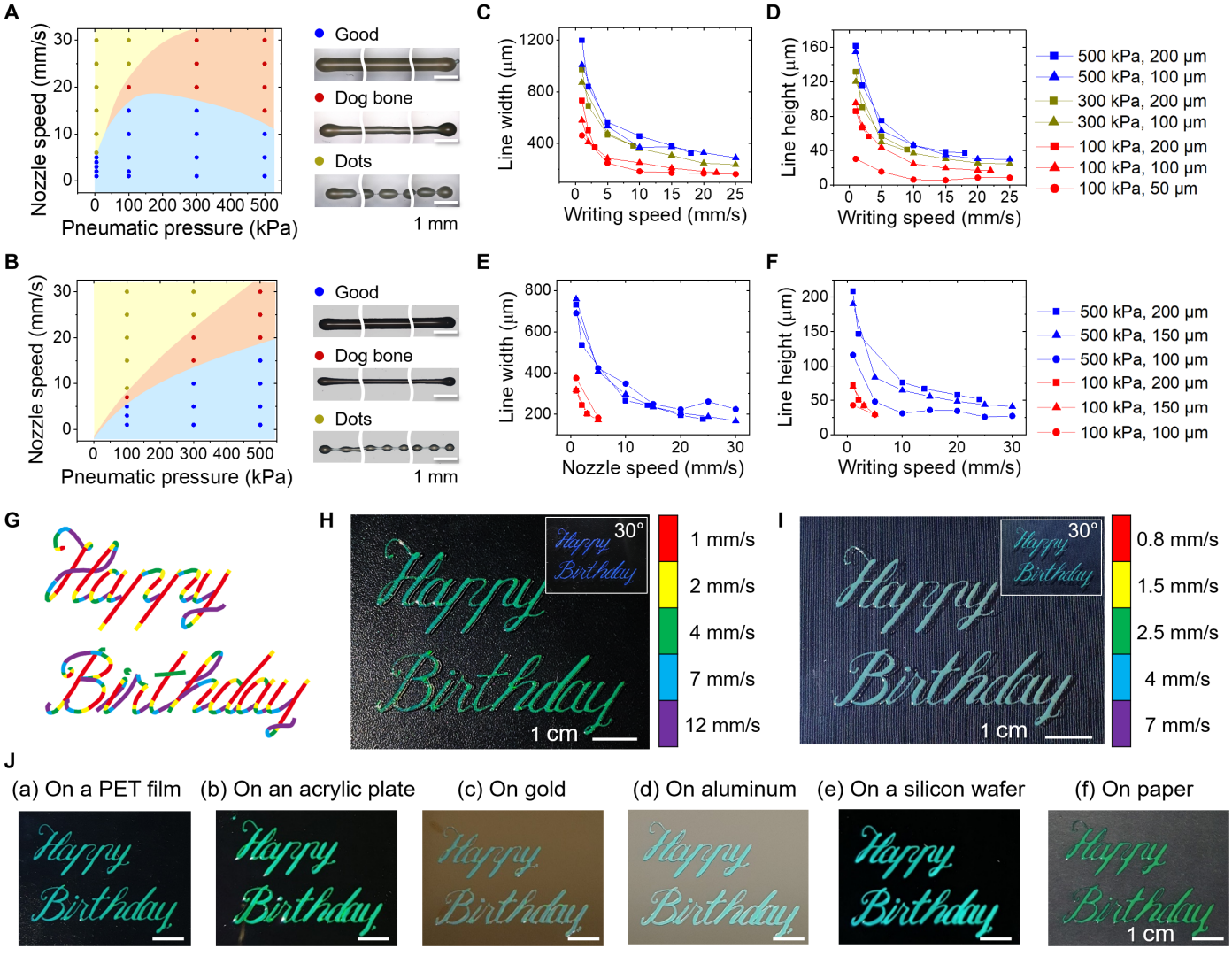

Fig. 2. Control over line dimensions. (**A**) Diagram for the formation of straight lines, dog bones, and a series of dots as a function of the writing speed and pneumatic pressure for EA inks. (**B**) Same set of subfigures shown in (A) but for UA inks. (**C** and **D**) Line width (C) and height (D) as a function of the writing speed for the denoted pneumatic pressures and gap distances for EA inks. (**E** and **F**) Same set of subfigures shown in (C) and (D) but for UA inks. (**G** to **I**) Dynamic control of the line width in the cursive "Happy Birthday" patterns for EA (H) and UA (I) inks; dynamic control was achieved by controlling the writing speed, as denoted with a color code (G). The insets are off-normal views for specular reflection where the incident and observation angles are 30° as denoted. (**J**) "Happy Birthday" patterns on various substrates: polyethylene terephthalate (PET) film (a), acrylic plate (b), gold (c), aluminum (d), silicon wafer (e), and paper (f). Photo credit: Jong Bin Kim, KAIST.

nozzle and the substrate so that the minimum width of lines after rapid spreading increases along with the gap; the minimum widths are 162, 174, and 371 μm for gap distances of 50, 100, and 200 μm, respectively. For the UA inks, by contrast, a smaller gap causes a larger contact of inks on the target surface at the moment of deposition, which results in wider lines; the minimum width is 225 μm for a gap of 100 and 176 μm for a gap of 200 μm. Because the narrower gap leads to greater hydrodynamic resistance, the ejection rate decreases along with the gap distance for a constant pneumatic pressure; the writing facilitates the ejection (fig. S22). Thermal annealing at 85°C for 10 min causes insignificant spreading of the lines for both the EA and UA inks.

The line width can be tuned in situ by adjusting the writing speed while maintaining the pneumatic pressure and gap distance. For example, the cursive text "Happy Birthday" is written by modulating the writing speed as programmed (Fig. 2G and movie S3). The pneumatic pressure and speeds are set to differ for the EA and UA inks to write the texts with the comparable variation of the line widths. As expected, the structural colors are highly angle dependent for the EA inks but are only slightly angle dependent for the UA inks (Fig. 2, H and I, and movie S4). The target surface is not restricted to glass. The graphics are drawn on various nonabsorbing surfaces of plastics, metals, and silicon wafers (Fig. 2J). The cross sections of lines are all arch-shaped, where the height-to-width ratio after thermal annealing is approximately 0.09, 0.08, 0.03, and 0.02 on glass, plastic, aluminum, and gold/silicon substrates for the EA inks and 0.12, 0.10, 0.04, and 0.04 for the UA inks, respectively (fig. S23). For absorbing surfaces, such as paper, a higher ejection rate or slower printing is required to compensate for the infiltration of the inks into voids (fig. S24).

Printing faces

The faces are formed by the fusion of lines drawn side by side (Fig. 3A). The inks are sufficiently fluidic to merge the lines but sufficiently viscous to remain where they are discharged. The lines are alternately drawn by displacing half the line width along the lateral direction. The second line is merged with the first one at the moment of drawing, and the lines from the third one are merged after the drawing. The merging initiates at the turning position, which rapidly progresses to heal the gap (movie S5). The zip-up speed is ~15 mm s^{-1}, which causes much faster fluid motion and, thus, greater shear stress along the lateral direction than the spreading of isolated lines. The surface profiles immediately before and after the merging are measured; from these measurements, the shear rate is estimated as 6.3 s^{-1} at the initial 0.13 and 2.7 s^{-1} at the next 0.33 s (Fig. 3B and fig. S25). Therefore, the dispersion near the substrate experiences a strong lateral shear flow, except for the first lines. The surfaces of the faces show a periodic thickness variation of 1.5 μm from the average for 57-μm-thick films immediately after the printing, which further decreases to almost zero within a few minutes by the action of capillary force (Fig. 3C) (*42*).

The as-printed faces are optically homogeneous, which gradually reveals color stripes along the direction of writing within 5 min at 85°C (Fig. 3D). The color stripes originate from the shear-induced crystallization by the fast merging. The stripes expand and cover the entire surface of the film as the crystal grows during the annealing process. The absolute reflectivity reaches 80% at the resonant wavelength in 10 min, although the refractive index contrast between the silica particles and the EA resin is as small as 0.02. For the UA inks, the films are optically homogeneous during the whole process of thermal incubation because no crystallization occurs (Fig. 3E). Nevertheless, the structural color and the reflectance peak become pronounced; the reflectivity is approximately 10%. The reflection colors from faces printed with EA inks are highly angle-dependent and directional, whereas those with UA inks are relatively less iridescent (figs. S26 and S27). Faces printed using the UA inks with $\phi \sim \phi_{th}$ exhibit crystallization during the annealing, where color stripes appear and merge in a manner similar to the color stripes in the EA inks (fig. S28). At low volume fractions, silica particles remain mobile, which facilitates crystallization; by contrast, the glass structure is kinetically arrested by ultralow mobility for the inks with $\phi \sim \phi_{opt}$.

The high reflectivity at the resonant wavelength for the faces printed using the EA ink originates from the high crystallinity and uniform crystal orientation in the entire film. Because the lateral shear stress strongly drives the particles to crystallize along the substrate, the trace of the string-like arrangement induced during the drawing is completely erased, and (111) planes of an fcc lattice are stacked along the thickness direction in the entire thermally annealed film, except the shear-free edges (Fig. 3F). Therefore, marked enhancement of color brightness and reflection peak intensity is observed for the fusion of more than two lines; no zip-up is observed until the second line (fig. S29). Notably, faces printed using the inks with $\phi < \phi_{opt}$ show a maximum reflectivity as low as 30% even after thermal annealing (fig. S30). Because the ink has a low viscosity, lines spread faster and wider than inks with $\phi = \phi_{opt}$, causing the lines to merge during the deposition. Therefore, there is no zip-up fusion, meaning that no strong shear force is available for rearrangement of the silica particles. Carbon black nanoparticles with the optimum concentration of 0.05% (w/w) in the ink hardly perturb the crystallization of silica particles, providing comparable reflectivity to the carbon black-free faces while enhancing color saturation through the suppression of incoherent scattering (fig. S31). Too high concentration, e.g., 0.2% (w/w), degrades the crystallinity and causes strong absorption, lowering color saturation and brightness.

Various color graphics can be drawn. For example, a quick response (QR) code is printed using green EA and UA inks (Fig. 3G). Each pixel in the code is constructed by the fusion of seven lines. Because the graphic is optically homogeneous, the direction of writing is not identified and the code is recognized by a smartphone (Fig. 3H). Images of Marilyn Monroe are also printed using the EA and UA inks (Fig. 3I). For the EA graphic with a crystalline structure, the reflection is reddish and the transmission is bluish for the incident beam at a low angle. The reflection color blue-shifts to green with the increasing angle, and the transmission color changes to magenta (Fig. 3J and movie S6).

Multicolor printing and potential uses

The high viscosity of the inks precludes the mixing of two different inks deposited in the same position even during thermal annealing as long as the ink medium is the same (fig. S32). That is, distinctively colored inks can be sequentially applied onto a single surface without photocuring (Fig. 4A). For example, the cursive text "Happy Birthday" is written using green EA ink over the face of red EA ink and using green UA ink over the face of blue UA ink without photocuring of the faces (Fig. 4B). When the inks with different mediums are brought into contact, the dissolution of one medium into the other leads to a change in particle volume fraction in the boundary, causing a color change and blurring the boundary (fig. S32). Black inks are respectively formulated by dispersing a large amount of black

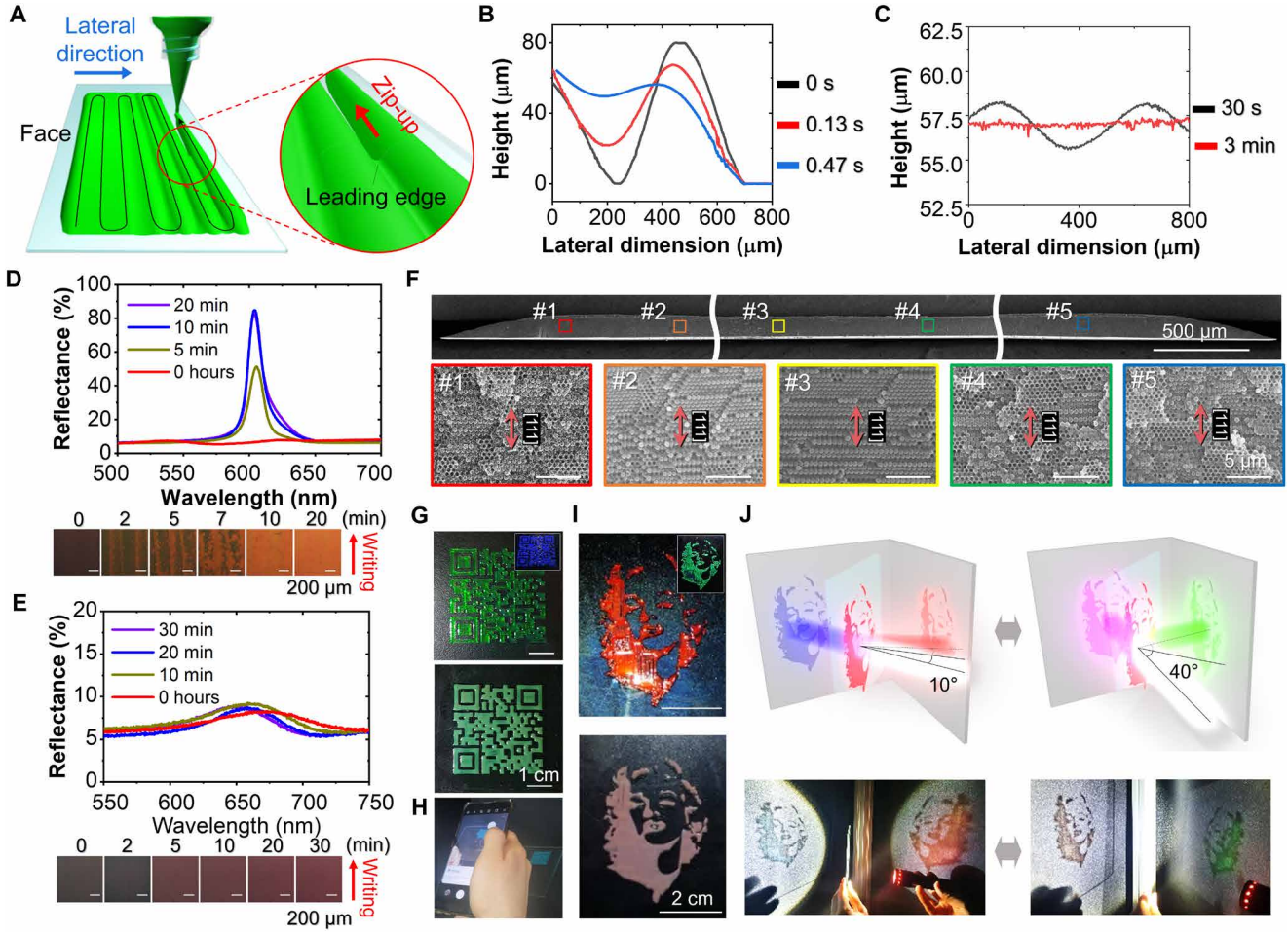

Fig. 3. Direct writing of structurally colored faces. (**A**) Schematic showing the formation of a face by fusion of alternately drawn lines, where the gap with an adjacent line is rapidly healed by zipping. (**B** and **C**) Rapid evolution of a surface profile by fusion (B) and gradual flattening of the surface (C). (**D**) Temporal evolutions of the reflectance spectrum and optical texture for a face drawn using an EA ink at 85°C. (**E**) Same set of images as in (D) but for a face drawn using UA ink. (**F**) Cross-sectional SEM images showing high flatness and thickness homogeneity and the uniform crystal orientation of the (111) plane along the top and bottom interfaces throughout the entire thickness. (**G** and **H**) QR code patterns produced using EA and UA inks (G) and recognition of the code with a smartphone (H). The inset is an off-normal observation. (**I** and **J**) Patterns of a Marilyn Monroe image produced using EA and UA inks (I) and projection of the images for reflection and transmission of the EA pattern at two different angles of illumination, as denoted (J). Photo credit: Jong Bin Kim, KAIST.

nanoparticles in the EA and UA inks containing silica particles with a diameter of 250 nm; the large silica particles do not show structural resonance in the visible region yet provide the desired rheological properties for printing. The black inks are printed over the patterns of color inks in the absence of color degradation (Fig. 4C). For example, graphics of a Morpho butterfly and a *Troides urvillianus* butterfly are printed using the blue EA and UA inks, where black EA and UA inks are additionally used, respectively (Fig. 4D); the Morpho butterfly exhibits sparkling blue with a regular structure, whereas the *T. urvillianus* exhibits matte blue with a random sphere-packing structure (*43*, *44*). Similarly, graphics of a red rose and green leaves are printed using the EA and UA inks, respectively, where black ink is deposited over the rose and leaf graphics to draw a contour (Fig. 4E). The rose and leaves drawn using the EA inks are strongly iridescent, whereas those drawn using the UA ink are not (movie S7). The Mickey Mouse graphic (Walt Disney, 1928) is drawn using five different inks: red ink for the pants; green ink for the shoes, black ink for the head, arms, and legs; white ink for the hands; and light-brown ink for the face (Fig. 4F and movie S8); the EA inks are used for the iridescent colors of the pants and shoes, whereas UA inks are used for matte colors. We formulate the white ink by dispersing large silica particles in the absence of carbon black and the light-brown ink by dispersing polydopamine nanoparticles instead of carbon black. The reflectance spectra and coordinates in CIE diagram for the distinct faces printed with all inks disclose the differences in colors and optical properties (figs. S33 and S34).

Single graphics can be produced with the EA and UA inks as long as the inks do not share a boundary. For example, the Golden Gate Bridge (San Francisco, CA, USA) graphic is drawn by sequential printing with six different inks: red EA for the main frame, green and blue EAs for the front and rear wires, blue UA for the bay, black UA for the footstone and parts of birds, and white UA for the wings of birds (Fig. 4G). All parts of the image are iridescent and transparent under the off-reflection condition, except the bay drawn with UA ink,

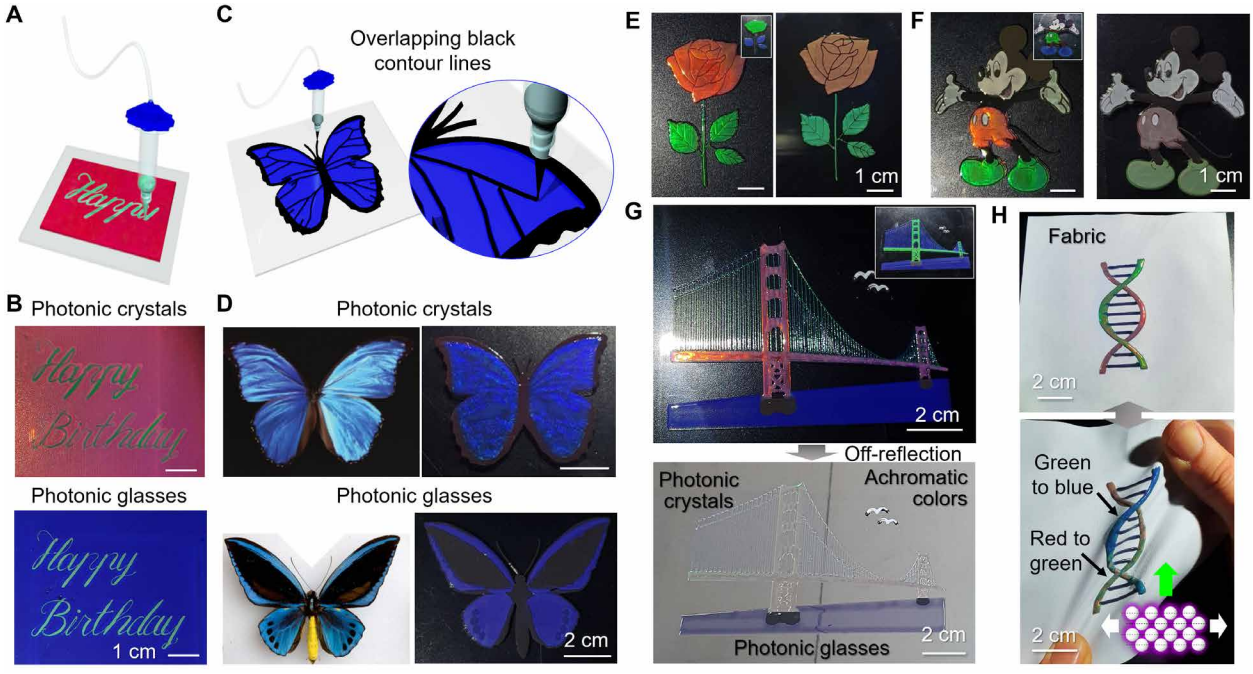

Fig. 4. Multicolor patterning. (**A** and **B**) Schematic (A) and photos (B) showing the overwriting of the cursive "Happy Birthday" using EA and UA inks on uncured faces of the same inks but with different colors. (**C** and **D**) Schematic for drawing black lines on structurally colored faces (C) and photos of a Morpho butterfly (top left) and a graphic drawn with EA ink (top right) and a *T. urvillianus* butterfly (bottom left) and a graphic drawn with UA ink (bottom right) (D). Reproduced with permission from (*43*) (2012 Wiley-VCH, top left) and (*44*) (2006 the Company of Biologists, bottom left). (**E**) A rose and leaves direct-written using EA and UA inks. The inset is an off-normal observation. (**F**) Mickey Mouse printed using EA and UA inks. (**G**) Golden Gate Bridge printed using both EA and UA inks for specular reflection and off-reflection with a white background. The bay drawn with UA ink is noniridescent and translucent, whereas other parts colored with EA inks are iridescent and transparent. (**H**) Nucleic acid double helix drawn on fabric using PEA inks. The insets show lattice deformation by stretching. Photo credit: Jong Bin Kim, KAIST.

which is consistent blue (movie S9). The PEA ink can form elastic graphics, resulting in dynamically tunable structural colors if the substrate is stretchable. For example, the nucleic acid double-helix structure is printed on white fabric using red and green PEA inks for the two strings of sugar phosphates and a blue PEA ink for the base pairs. To compensate for the penetration of the inks into the voids of the fabric, the PEA inks are deposited in excess. The helix shows a blue shift of the colors when the fabric is stretched, which reduces the interparticle distance along the thickness direction (Fig. 4H) (*45*, *46*).

After photocuring, the direct-written graphics exhibit sufficient mechanical stability to be detached from the substrates as freestanding films. For example, a chameleon pattern drawn with red, green, and black PEA inks is released from a glass substrate and then transferred onto an elastic silicone film. The chameleon shows a reversible color change when stretched and relaxed (Fig. 5, A and B, and movie S10). The elastic films made of PEA inks have Young's modulus as small as 1.40 MPa, and tensile strain at fracture is $\varepsilon = 0.67$ (fig. S35A). The graphics drawn with UA inks are tough, enabling them to be folded without fracturing; Young's modulus is 39.3 MPa, tensile strain at fracture is $\varepsilon = 0.51$, and the minimum radius of curvature before fracture is as small as 0.2 mm (fig. S35B). For example, red, green, and blue patches are printed on paper using three distinct UA inks, and the paper is folded multiple times to make a bird through origami, without the graphic cracking (Fig. 5, C and D). Also, a planar figure of a soccer ball with red, green, and blue pentagons is printed on glass using UA inks; the graphic is subsequently detached from the glass and attached to the surface of a glass bead using an adhesive (Fig. 5, E and F). The films printed with EA inks are rigid, which have Young's modulus of 243 MPa. The tensile strain at fracture is $\varepsilon = 0.093$, and the minimum radius of curvature is 11.8 mm (fig. S35C).

DISCUSSION

We demonstrate the direct writing of structurally colored graphics using viscoelastic photonic inks. The inks are optimally formulated to simultaneously achieve the macroscopic rheological properties desired for high printability and the microscopic colloidal arrangement desired for structural coloration. The colloidal arrangement is governed by the viscosity of the ink medium to be either a crystalline structure for iridescent colors or a glassy structure for less-iridescent colors. Direct writing provides structurally colored lines with controlled width in the range of 180 to 800 μm, where the printing speed can be increased up to 15 mm s^{-1} without compromising the printing quality. The fusion of the lines produces faces with controlled crystal orientation and high flatness, which show absolute reflectivity higher than 80%. Because a high viscosity precludes the mixing of two distinct inks, multicolored graphics are printed with single-step photocuring. Moreover, the graphics can be directly printed on various target surfaces, including glasses, plastics, metals, paper, and fabrics, or transferred onto any target surface.

This pragmatic direct-writing approach provides unprecedented levels of controllability and versatility, serving as the practical means to design structural color graphics. First, color graphics can be tailored by customers and printed on apparel and accessories for fashions.

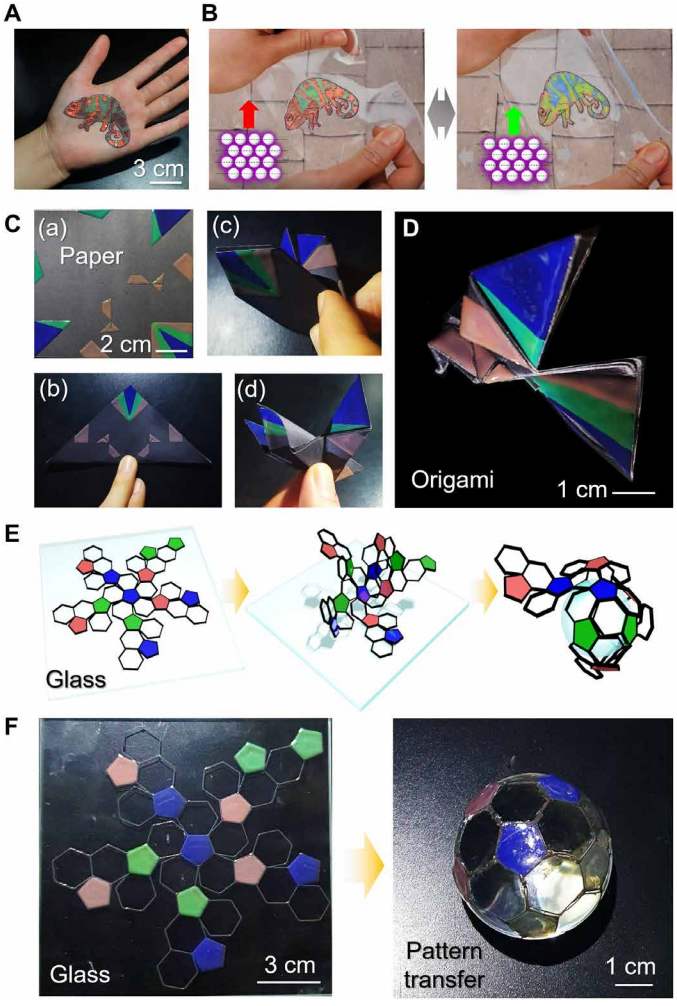

Fig. 5. Multicolor patterns with controlled properties. (**A** and **B**) Photos of a chameleon pattern printed using PEA inks (A) and its reversible color change when stretched and relaxed (B). (**C** and **D**) Photos of the color pattern printed on paper using UA inks and its origami process (C) to make a bird (D). (**E** and **F**) Schematics (E) and photos (F) showing the planar figure for a soccer ball printed using UA inks to transfer onto the surface of a glass sphere. Photo credit: Jong Bin Kim, KAIST.

In particular, color patterns can be inserted onto contact lenses without chemical pigments, like natural blue eyes, which provide nontoxic yet aesthetic colors (*47*). Second, twinkling and iridescent colors and unique shape of the reflectance spectrum featured by a sharp single peak are not copiable, enabling the graphics to function as customizable anticounterfeiting patterns for art masterpieces and top-secret documents (*48*). Third, the conspicuous and highly visible colors are promising for signboards and advertisements (*20*, *28*). Fourth, the high chemical and thermal stability of the structural colors is appealing for preserving information under harsh environments in which chemical pigments are vulnerable (*49*, *50*). The photonic inks can be further formulated to have various stimuli responsiveness (*51*). The color-tunable graphics on fabrics can be used as wearable displays similar to chameleon skin. Stimuli-responsive patches are used as intuitive colorimetric indicators for temperature, humidity, pH, and specific molecules in our daily life and industry.

MATERIALS AND METHODS

Preparation of photonic inks

Monodisperse silica particles with average diameters of 145, 175, 190, 226, and 250 nm (Sukgyung AT) were weighed and subsequently dispersed in ethanol by sonication overnight. Carbon black nanoparticles with an average diameter of 24 nm (Hiblack 420B, Korea Carbon Black Co.) were dispersed in resins of ethoxylated trimethylolpropane triacrylate (M_n ~ 428 g mol^{-1}, Sigma-Aldrich), poly(ethylene glycol) PEA (M_n ~ 324 g mol^{-1}, Sigma-Aldrich), and polyurethane acrylate (PU2100, M_n ~ 1400 g mol^{-1}, Miwon Chemicals) containing 1% (w/w) 2-hydroxy-2-methylpropiophenone (Sigma-Aldrich) photoinitiator at a concentration of 0.05% (w/w) in a silica-free resin basis. The resin was added to the ethanolic dispersions of silica particles and sonicated for 10 min. The mixture was kept in a convection oven overnight to completely evaporate ethanol. The resultant dispersions were vigorously mixed using a planetary centrifugal mixer (AR-310, Thinky). For white inks, silica particles with an average diameter of 250 nm were used. Black and brown inks were formulated by dispersing 1% (w/w) carbon black nanoparticles and 0.28% (w/w) polydopamine nanoparticles with an average diameter of 91 nm in the white inks, respectively.

Direct writing

The inks were discharged through a plastic nozzle using a dispensing system with an automated stage (Image Master 350PC Smart, Musashi Engineering). The nozzle had a 200-μm orifice and a 100-μm-thick wall at the tip. The pneumatic pressure was controlled in the range of 1 to 500 kPa by an ML-5000XII valve controller (Musashi Engineering). The trajectory and speed of writing were programmed in the MUCADV software (Musashi Engineering). Original images were imported into the MUCADV or AutoCAD (Autodesk) and subsequently coded by line segments. The writing speed was manually set on the basis of the relation between the line width and the speed. As target surfaces, slide glasses (Paul Marienfeld GmbH & Co. KG), polyethylene terephthalate (PET) films (DuPont Teijin Films), acrylic plates, gold, aluminum, silicon wafer (Sehyoung Wafertech), and paper are used without a cleaning process. The patterns were cured by irradiation with UV (MPS-306F, Coolwave) under a nitrogen atmosphere.

Analysis of rheological properties

The rheological properties of the inks were analyzed using a rheometer (MCR 101, Anton Parr). A plate-to-plate geometry was used for EA inks with a volume fraction of silica particles of 40% (v/v) or greater and UA inks with a fraction of 30% (v/v) or greater, whereas a Couette geometry was used for the EA and UA inks with lower fractions. Oscillatory tests for measuring the storage and loss moduli were carried out in both strain- and stress-controlled modes. In the strain-controlled mode, the shear rate was varied in the range of 0.1 to 100 rad s^{-1} through frequency sweeping, where the strain amplitude was fixed at 5%. For the stress-controlled mode, the shear stress was varied in the range of 0.01 to 100 Pa through an amplitude sweep, where the frequency was fixed at 1 Hz. Viscosity was measured for shear rates spanning 0.0001 to 100 s^{-1}. A thixotropy test was conducted between low and high shear rates, where the low shear rate was set to 0.001 s^{-1} and the high shear rates were set to 0.1, 1, 10, and 25 s^{-1}. Before each measurement, to erase any history, the inks were sheared at a rate of 1 s^{-1} for 1 min and then left shear free for 2 min.

Characterization

The graphics designed by direct writing were imaged with consumer-grade digital cameras and observed by optical microscopy in reflection mode (Eclipse L150, Nikon). The reflectance spectra were recorded using a fiber-coupled spectrometer (USB 4000, Ocean Optics) installed in a microscope with a 10× lens, where a broadband dielectric mirror (BB3-E02, Thorlabs) is used as a reference. The arrangement of silica particles in photocured inks was observed by scanning electron microscopy (SEM; S-4800, Hitachi) after the specimens were coated with osmium. The surface profiles were measured using optical profilometry (Nanofocus AG, Germany).

SUPPLEMENTARY MATERIALS

Supplementary material for this article is available at https://science.org/doi/10.1126/sciadv.abj8780

REFERENCES AND NOTES

1. A. Sweeney, C. Jiggins, S. Johnsen, Polarized light as a butterfly mating signal. *Nature* **423**, 31–32 (2003).
2. J. Teyssier, S. V. Saenko, D. Van Der Marel, M. C. Milinkovitch, Photonic crystals cause active colour change in chameleons. *Nat. Commun.* **6**, 6368 (2015).
3. M. Jacobs, M. Lopez-Garcia, O.-P. Phrathep, T. Lawson, R. Oulton, H. M. Whitney, Photonic multilayer structure of *Begonia* chloroplasts enhances photosynthetic efficiency. *Nat. Plants* **2**, 16162 (2016).
4. M. Lopez-Garcia, N. Masters, H. E. O'Brien, J. Lennon, G. Atkinson, M. J. Cryan, R. Oulton, H. M. Whitney, Light-induced dynamic structural color by intracellular 3D photonic crystals in brown algae. *Sci. Adv.* **4**, eaan8917 (2018).
5. E. Armstrong, C. O'Dwyer, Artificial opal photonic crystals and inverse opal structures–fundamentals and applications from optics to energy storage. *J. Mater. Chem. C* **3**, 6109–6143 (2015).
6. S.-H. Kim, S. Y. Lee, S.-M. Yang, G.-R. Yi, Self-assembled colloidal structures for photonics. *NPG Asia Mater.* **3**, 25–33 (2011).
7. P. Jiang, J. Bertone, K. S. Hwang, V. Colvin, Single-crystal colloidal multilayers of controlled thickness. *Chem. Mater.* **11**, 2132–2140 (1999).
8. Y. Takeoka, Angle-independent structural coloured amorphous arrays. *J. Mater. Chem.* **22**, 23299–23309 (2012).
9. Y. Takeoka, M. Honda, T. Seki, M. Ishii, H. Nakamura, Structural colored liquid membrane without angle dependence. *ACS Appl. Mater. Interfaces* **1**, 982–986 (2009).
10. J. Hou, M. Li, Y. Song, Patterned colloidal photonic crystals. *Angew. Chem. Int. Ed.* **57**, 2544–2553 (2018).
11. J. B. Kim, S. Y. Lee, J. M. Lee, S.-H. Kim, Designing structural-color patterns composed of colloidal arrays. *ACS Appl. Mater. Interfaces* **11**, 14485–14509 (2019).
12. E. Kim, Y. Xia, G. M. Whitesides, Two- and three-dimensional crystallization of polymeric microspheres by micromolding in capillaries. *Adv. Mater.* **8**, 245–247 (1996).
13. Z. Z. Gu, A. Fujishima, O. Sato, Patterning of a colloidal crystal film on a modified hydrophilic and hydrophobic surface. *Angew. Chem. Int. Ed.* **114**, 2171–2174 (2002).
14. S. M. Yang, H. Miguez, G. A. Ozin, Opal circuits of light—planarized microphotonic crystal chips. *Adv. Funct. Mater.* **12**, 425–431 (2002).
15. A. T. Tan, J. Beroz, M. Kolle, A. J. Hart, Direct-write freeform colloidal assembly. *Adv. Mater.* **30**, 1803620 (2018).
16. A. T. Tan, S. Nagelberg, E. Chang-Davidson, J. Tan, J. K. Yang, M. Kolle, A. J. Hart, In-plane direct-write assembly of iridescent colloidal crystals. *Small* **16**, 1905519 (2020).
17. H. S. Lee, T. S. Shim, H. Hwang, S.-M. Yang, S.-H. Kim, Colloidal photonic crystals toward structural color palettes for security materials. *Chem. Mater.* **25**, 2684–2690 (2013).
18. S. Y. Lee, S. H. Kim, H. Hwang, J. Y. Sim, S. M. Yang, Controlled pixelation of inverse opaline structures towards reflection-mode displays. *Adv. Mater.* **26**, 2391–2397 (2014).
19. M. Schaffner, G. England, M. Kolle, J. Aizenberg, N. Vogel, Combining bottom-up self-assembly with top-down microfabrication to create hierarchical inverse opals with high structural order. *Small* **11**, 4334–4340 (2015).
20. K. Chen, Q. Fu, S. Ye, J. Ge, Multicolor printing using electric-field-responsive and photocurable photonic crystals. *Adv. Funct. Mater.* **27**, 1702825 (2017).
21. I. B. Burgess, L. Mishchenko, B. D. Hatton, M. Kolle, M. Loncar, J. Aizenberg, Encoding complex wettability patterns in chemically functionalized 3D photonic crystals. *J. Am. Chem. Soc.* **133**, 12430–12432 (2011).
22. Y. Wang, D. Aurelio, W. Li, P. Tseng, Z. Zheng, M. Li, D. L. Kaplan, M. Liscidini, F. G. Omenetto, Modulation of multiscale 3D lattices through conformational control: Painting silk inverse opals with water and light. *Adv. Mater.* **29**, 1702769 (2017).
23. J. Park, J. Moon, H. Shin, D. Wang, M. Park, Direct-write fabrication of colloidal photonic crystal microarrays by ink-jet printing. *J. Colloid Interface Sci.* **298**, 713–719 (2006).
24. L. Bai, Z. Xie, W. Wang, C. Yuan, Y. Zhao, Z. Mu, Q. Zhong, Z. Gu, Bio-inspired vapor-responsive colloidal photonic crystal patterns by inkjet printing. *ACS Nano* **8**, 11094–11100 (2014).
25. K. Keller, A. V. Yakovlev, E. V. Grachova, A. V. Vinogradov, Inkjet printing of multicolor daylight visible opal holography. *Adv. Funct. Mater.* **28**, 1706903 (2018).
26. L. Bai, V. C. Mai, Y. Lim, S. Hou, H. Möhwald, H. Duan, Large-scale noniridescent structural color printing enabled by infiltration-driven nonequilibrium colloidal assembly. *Adv. Mater.* **30**, 1705667 (2018).
27. S. H. Kim, J. M. Lim, W. C. Jeong, D. G. Choi, S. M. Yang, Patterned colloidal photonic domes and balls derived from viscous photocurable suspensions. *Adv. Mater.* **20**, 3211–3217 (2008).
28. M. Kuang, J. Wang, B. Bao, F. Li, L. Wang, L. Jiang, Y. Song, Inkjet printing patterned photonic crystal domes for wide viewing-angle displays by controlling the sliding three phase contact line. *Adv. Opt. Mater.* **2**, 34–38 (2014).
29. R. Shanker, S. Sardar, S. Chen, S. Gamage, S. Rossi, M. P. Jonsson, Noniridescent biomimetic photonic microdomes by inkjet printing. *Nano Lett.* **20**, 7243–7250 (2020).
30. V. G. Rocha, E. Saiz, I. S. Tirichenko, E. García-Tuñón, Direct ink writing advances in multi-material structures for a sustainable future. *J. Mater. Chem. A* **8**, 15646–15657 (2020).
31. B. Konijn, O. Sanderink, N. P. Kruyt, Experimental study of the viscosity of suspensions: Effect of solid fraction, particle size and suspending liquid. *Powder Technol.* **266**, 61–69 (2014).
32. O. L. Pursiainen, J. J. Baumberg, H. Winkler, B. Viel, P. Spahn, T. Ruhl, Nanoparticle-tuned structural color from polymer opals. *Opt. Express* **15**, 9553–9561 (2007).
33. H. Cong, B. Yu, S. Wang, L. Qi, J. Wang, Y. Ma, Preparation of iridescent colloidal crystal coatings with variable structural colors. *Opt. Express* **21**, 17831–17838 (2013).
34. N. J. Wagner, J. F. Brady, Shear thickening in colloidal dispersions. *Phys. Today* **62**, 27–32 (2009).
35. F. E. Mackay, K. Pastor, M. Karttunen, C. Denniston, Modeling the behavior of confined colloidal particles under shear flow. *Soft Matter* **10**, 8724–8730 (2014).
36. Y. Li, Q. Fan, X. Wang, G. Liu, L. Chai, L. Zhou, J. Shao, Y. Yin, Shear-induced assembly of liquid colloidal crystals for large-scale structural coloration of textiles. *Adv. Funct. Mater.* **31**, 2010746 (2021).
37. Y. Eom, F. Kim, S. E. Yang, J. S. Son, H. G. Chae, Rheological design of 3D printable all-inorganic inks using BiSbTe-based thermoelectric materials. *J. Rheol.* **63**, 291–304 (2019).
38. K. Ueno, S. Imaizumi, K. Hata, M. Watanabe, Colloidal interaction in ionic liquids: Effects of ionic structures and surface chemistry on rheology of silica colloidal dispersions. *Langmuir* **25**, 825–831 (2009).
39. G. J. Donley, P. K. Singh, A. Shetty, S. A. Rogers, Elucidating the G″ overshoot in soft materials with a yield transition via a time-resolved experimental strain decomposition. *Proc. Natl. Acad. Sci.* **117**, 21945–21952 (2020).
40. T. Besseling, M. Hermes, A. Fortini, M. Dijkstra, A. Imhof, A. Van Blaaderen, Oscillatory shear-induced 3D crystalline order in colloidal hard-sphere fluids. *Soft Matter* **8**, 6931–6939 (2012).
41. X. Cheng, X. Xu, S. A. Rice, A. R. Dinner, I. Cohen, Assembly of vorticity-aligned hard-sphere colloidal strings in a simple shear flow. *Proc. Natl. Acad. Sci.* **109**, 63–67 (2012).
42. P.-G. de Gennes, F. Brochard-Wyart, D. Quéré, Hydrodynamics of interfaces: Thin films, waves, and ripples, in *Capillarity and Wetting Phenomena: Drops, Bubbles, Pearls, Waves* (Springer, New York, ed. 1, 2004), pp.112–115.
43. K. Chung, S. Yu, C. J. Heo, J. W. Shim, S. M. Yang, M. G. Han, H. S. Lee, Y. Jin, S. Y. Lee, N. Park, J. H. Shin, Flexible, angle-independent, structural color reflectors inspired by Morpho butterfly wings. *Adv. Mater.* **24**, 2375–2379 (2012).
44. R. O. Prum, T. Quinn, R. H. Torres, Anatomically diverse butterfly scales all produce structural colours by coherent scattering. *J. Exp. Biol.* **209**, 748–765 (2006).
45. G. H. Lee, T. M. Choi, B. Kim, S. H. Han, J. M. Lee, S.-H. Kim, Chameleon-inspired mechanochromic photonic films composed of non-close-packed colloidal arrays. *ACS Nano* **11**, 11350–11357 (2017).
46. R. Hong, Y. Shi, X.-Q. Wang, L. Peng, X. Wu, H. Cheng, S. Chen, Highly sensitive mechanochromic photonic gel towards fast- responsive fingerprinting. *RSC Adv.* **7**, 33258–33262 (2017).
47. J. Deng, S. Chen, J. Chen, H. Ding, D. Deng, Z. Xie, Self-reporting colorimetric analysis of drug release by molecular imprinted structural color contact lens. *ACS Appl. Mater. Interfaces* **10**, 34611–34617 (2018).
48. M. Pan, L. Wang, S. Dou, J. Zhao, H. Xu, B. Wang, L. Zhang, X. Li, L. Pan, Y. Li, Recent advances in colloidal photonic crystal-based anti-counterfeiting materials. *Crystals* **9**, 417 (2019).

49. F. Li, B. Tang, S. Wu, W. Ma, S. Zhang, Bright structural coloration from organic polymeric photonic crystals with robust heat-resistance. *J. Mater. Chem. C* **5**, 9806–9811 (2017).
50. W. Niu, X. Wang, Y. Zheng, S. Wu, M. Hua, Y. Wang, X. Zhang, A. I. Y. Tok, X. He, S. Zhang, Inorganic photonic microspheres with localized concentric ordering for deep pattern encoding and triple sensory microsensor. *Small* **16**, 2003638 (2020).
51. M. Qin, M. Sun, M. Hua, X. He, Bioinspired structural color sensors based on responsive soft materials. *Curr. Opin. Solid State Mater. Sci.* **23**, 13–27 (2019).

Acknowledgments
Funding: This research was supported by KoreaToray Science Foundation and the National Research Foundation (NRF-2018M3A7B8060189). **Author contributions:** S.-H.K. and J.B.K. conceived the idea and designed the experiment. J.B.K. performed the experiments and analyzed the data. C.C. and S.Y.L. assisted with the characterization of rheological properties and printing. S.H.H. synthesized the polydopamine nanoparticles. J.B.K. and S.-H.K. wrote the manuscript. S.-H.K. supervised the project. All the authors read the manuscript, discussed it, and approved its content. **Competing interests:** J.B.K., S.H.H., and S.H.K. are inventors on a patent application relating to the strategy described in this work. All other authors declare that they have no competing interests. **Data and materials availability:** All data needed to evaluate the conclusions in the paper are present in the paper and/or the Supplementary Materials.

Submitted 9 June 2021
Accepted 4 October 2021
Published 24 November 2021
10.1126/sciadv.abj8780